HOKKAIDO UNIVERSITY

| | |
|---|---|
| Title | Trigger of the Highly Resistive Layer Formation at the Cathode-Electrolyte Interface in All-Solid-State Lithium Batteries Using a Garnet-Type Lithium-Ion Conductor |
| Author(s) | Onoue, Kana; Nasu, Akira; Matsumoto, Kazuhiko et al. |
| Citation | ACS applied materials & interfaces, 15(45), 52333-52341<br>https://doi.org/10.1021/acsami.3c07177 |
| Issue Date | 2023-11-15 |
| Doc URL | https://hdl.handle.net/2115/93595 |
| Rights | This document is the Accepted Manuscript version of a Published Work that appeared in final form in ACS applied materials & interfaces, copyright © 2023 American Chemical Society after peer review and technical editing by the publisher. To access the final edited and published work see https://pubs.acs.org/articlesonrequest/AOR-HH4NPFMIAACWZGGFK |
| Type | journal article |
| File Information | 02_Onoue_LCOLLZTO_Revised3.pdf |

Hokkaido University Collection of Scholarly and Academic Papers : HUSCAP

# Trigger of the Highly Resistive Layer Formation at Cathode-Electrolyte Interface in All-Solid-State Lithium Batteries Using Garnet-type Lithium Ion Conductor

*Kana Onoue[1], Akira Nasu[1, 2], Kazuhiko Matsumoto[3], Rika Hagiwara[3], Hiroaki Kobayashi[1, 2], and Masaki Matsui[1, 2*]*

1. Graduate School of Chemical Science and Engineering, Hokkaido University, Sapporo, 060-0810, Japan
2. Department of Chemistry, Hokkaido University, Sapporo, 060-0810, Japan
3. Graduate School of Energy Science, Kyoto University, Kyoto, 606-8501, Japan

*Corresponding Author

Masaki Matsui

e-mail: matsui@sci.hokudai.ac.jp

KEYWORD

Solid state electrolyte, Garnet, Phase separation, Interfacial reaction, chemical potential

ABSTRACT

Interfacial materials design is critical in the development of all-solid-state lithium batteries. We must develop an electrode–electrolyte interface with low resistance and effectively utilize the energy stored in the battery system. Here we investigated the highly resistive layer formation process at the interface of a layered cathode: $LiCoO_2$, and a garnet-type solid-state electrolyte: $Li_{6.4}La_3Zr_{1.4}Ta_{0.6}O_{12}$, during the co-sintering process using in-situ/ex-situ high-temperature X-ray diffraction. The onset temperature of the reaction between a lithium-deficient $Li_xCoO_2$ and $Li_{6.4}La_3Zr_{1.4}Ta_{0.6}O_{12}$ is 60 °C, while a stoichiometric $LiCoO_2$ does not show any reaction up to 900 °C. The chemical potential gap of lithium first triggers the lithium migration from the garnet phase to the $Li_xCoO_2$ below 200 °C. The lithium-extracted garnet gradually decomposes around 200 °C and mostly disappears at 500 °C. Since the interdiffusion of the transition metal is not observed below 500 °C, the early-stage reaction product is the decomposed lithium-deficient garnet phase. Electrochemical impedance spectroscopy results showed that the highly resistive layer is formed even below 200 °C. The present work offers that the origin of the highly resistive layer formation is triggered by lithium migration at the solid-solid interface and decomposition of the lithium-deficient garnet phase. We must prevent spontaneous lithium migration at the cathode-electrolyte interface to avoid highly resistive layer formation. Our results show that the lithium chemical potential gap should be the critical parameter for designing an ideal solid-solid interface for all-solid-state battery applications.

INTRODUCTION

All-solid-state lithium batteries, consisting of electrodes and non-flammable solid-state electrolytes, exhibit significant advantages over lithium-ion batteries in terms of safety and energy

density[1]. Among possible choices for the solid-state electrolytes, garnet-type lithium-ion conductor $Li_7La_3Zr_2O_{12}$(LLZO)[2] and its derivatives[3] are promising materials due to their relatively high conductivities (in cubic phase, up to $10^{-3}$ $Scm^{-1}$). Furthermore, their wide theoretical electrochemical window enables us to use a high-voltage cathode and lithium metal anode. Nevertheless, there are critical issues with interface formation for smooth charge transfer between the solid-solid interfaces of the garnets and lithium metal or oxide cathode materials. The biggest challenge in the development of the all-solid-state lithium batteries using the garnet-type lithium ion conductor is the formation of the cathode-electrolyte interface.[4–11]

The high-temperature sintering process, generally employed for ceramic capacitor production, is necessary to form a smooth interfacial junction between the cathode and electrolyte. However, the co-sintering process of the cathode active material and solid-state electrolyte leads to side reactions at the solid-solid interface resulting in poor electrochemical properties.[4,12] A computational study predicted that the layered oxide cathode, such as $LiCoO_2$(LCO) with LLZO interfaces, is more stable than other transition metal cations in the cathode ($LiMn_2O_4$ and $LiNi_{0.3}Mn_{0.3}Co_{0.3}O_2$)[13]. Vardar et al. identified that the most likely reaction products at the interface are $La_2Zr_2O_7$ and $LaCoO_3$ due to annealing up to 500 °C [10]. On the other hand, theoretical studies have predicted no decomposition products between garnets and LCO [13]. This prediction does not match well with experimental findings. We must remember that the discrepancy comes from the sintering temperature and environment, which is not considered in those calculations. In the previous study, the decomposition layer, arising from the thermodynamic driving force such as thermal treatment, is recognized to be the non-conducting phase via transition metal diffusion at high temperatures[5,7–10]. Decreasing the sintering temperature is the most straightforward solution to suppress the side reactions, and thus various sintering strategies were attempted to

improve electrochemical properties.[14–19] However, the electrochemical properties are degraded even at 350 °C, below the detectable temperature of the reaction layer[4]. This means that other factors contribute to the degradation of electrochemical properties besides the transition metal diffusion. We suspect that the interdiffusion of lithium ions rather than transition metal ions triggers the highly resistive layer formation at the electrode-electrolyte interface.

Recent studies have revealed that surface coating by $LiNbO_3$(LNO) at the solid electrolyte-cathode interface successfully prevents the interdiffusion of the transition metals on thermal treatment and decreases interfacial resistances experimentally [20–22]. Bo et al. reported that computational analysis of the LCO-LNO-β-$Li_3PS_4$ solid electrolyte interfaces provides a reliable explanation for the effectiveness of the coating layer[23]. The LNO coating effectively decreases the interfacial resistance by reducing the $Li^+$ electrochemical potential gap at the cathode electrolyte interface, which also partially acts as the migration barrier of $Li^+$ ions. Despite the importance of understanding the transport behavior of $Li^+$ ions at the solid-solid interface, there is no experimental demonstration to investigate the influence of lithium migration on the highly resistive layer formation process. Accordingly, we focused on the migration behavior of lithium ions at the solid-solid interface. We investigated the highly resistive layer formation process using a model interface that facilitates lithium migration.

In the present study, we attempted to determine the critical parameters of the highly resistive layer formation process. We examined the chemical degradation mechanisms of the LCO-LLZTO interface during thermal treatments. We reveal that the lithium migration at the cathode-electrolyte interface triggers the formation of the highly resistive layer. We compared the reactions of LLZTO with a stoichiometric $LiCoO_2$ and a chemically delithiated $LiCoO_2$($Li_xCoO_2$, LxCO), which must have different Li chemical potential gaps ($\Delta\mu_{Li}$). High-temperature in-situ XRD measurements

revealed that the phase separation of LLZTO is triggered at a much lower temperature than in previous reports, with a detrimental impact on the interface resistance. Our findings in the present work propose desirable materials design strategies at the solid-solid interface, particularly preventing lithium extraction from LLZTO during the cathode-electrolyte interface formation.

## EXPERIMENTAL PROCEDURE

### Synthesis of $Li_{6.4}La_3Zr_{1.4}Ta_{0.6}O_{12}$ and delithiated $LiCoO_2$

The garnet-type lithium ion conductor $Li_{6.4}La_3Zr_{1.4}Ta_{0.6}O_{12}$(LLZTO) is synthesized via a conventional solid-state reaction. Stoichiometric amounts of $LiOH{\cdot}H_2O$ (Nacalai Tesque, ≥99.0%), $La(OH)_3$ (Wako, ≥99.9%), $ZrO_2$ (Tosoh), and $Ta_2O_5$ (Wako, ≥99.9%) were mixed with excess $LiOH{\cdot}H_2O$ of 10 wt.% to compensate for the lithium evaporation during the sintering process. The starting materials were grounded and mixed using a planetary ball milling (Pulverisette 7, Fritsch, Germany) with zirconia milling media in acetone for 2 hours, followed by a drying process. The mixed powder was sieved through a 600 μm sieve and pelletized at 354 MPa. The pellets were placed on a gold sheet and confined in a crucible with a lid for calcination. Subsequently the pellets were calcined in an electric furnace (Electric Furnace 300-plus, Denken-Hydenthal) in the ambient atmosphere at 900 °C for 12 hours at a heating rate of 10 °C $min^{-1}$. The crucible with pellets was removed from the furnace at 500 °C, immediately transferred to an antechamber of a glove box, and cooled it down to room temperature under vacuum to avoid reactions with moisture or $CO_2$[24]. Figure S1 shows the powder XRD patterns of synthesized LLZTO. All the observed peaks correspond to cubic LLZTO (ICDD PDF 04-018-9024).

Delithiated $LiCoO_2$ was prepared by chemical oxidation of LCO (>=99.0%, Japan Chemical Industry) using chlorine gas following the procedure reported in Ref [25]. An LCO powder is

immersed in acetonitrile and delithiated with chlorine gas in the presence of $AlCl_3$, based on the following equation (1).

$$LiCoO_2 + xAlCl_3 + \frac{x}{2}Cl_2 \rightarrow Li_{1-x}CoO_2 + xLiAlCl_4 \quad (1)$$

Chlorine gas acts as an oxidizing agent (4.40 V vs. Li+/Li), and $AlCl_3$ acts as a Lewis acid to dissolve the LiCl on the surface of LCO. Into an air-tight glass flask (~1.19 $dm^3$) with a glass lid equipped with a value, 10.0 g of LCO (0.102 mol), 13.6 g of $AlCl_3$ (0.102 mol), and 75 mL acetonitrile were added under a dry Ar atmosphere. After the glass flask was connected to the reaction line and the Ar gas inside was pumped off, 50 kPa of chloride gas (~24.0 mmol) was slowly introduced from a storage cylinder. After agitation of 24 hours, the residual chlorine gas was pumped out. 9.28 g of the final product was obtained by washing with acetonitrile, centrifugation (3 times), and solvent removal under vacuum. The obtained products were characterized as $Li_xCoO_2$ (x=0.55) by XRD analysis in Fig. S2. The lithium content in LxCO was determined by the 003 peak position.

Sample preparation and characterization

The LLZTO powder was mixed with an LCO (or LxCO) in a mass ratio 1:1 using a mortar and pestle. The mixture was pressed into pellets under 354 MPa to ensure good contact among particles. The pellets were calcined at 60–900 °C for 12 hours under an argon atmosphere.

Structural characterizations of samples were performed using an X-ray diffractometer (D8 Advance, Bruker) equipped with Cu Kα radiation operating at 40 kV and 40 mA. All the Ex-situ XRD measurements were carried out using an airtight sample holder to avoid air exposure. In-situ

XRD measurements were carried out using a high-temperature chamber (HTK-1200, Anton Parr) in a temperature range of 60–900 °C under Ar flow with 3 hours of temperature holding time before each measurement. Surface morphology was observed using FE-SEM (JSM-6335F, JEOL), and elemental mapping was performed by EDX (JED-2200, JEOL).

Electrochemical Measurement

An OCV measurement was performed to estimate $\mu_{Li}$ gap between LLZTO and LCO. Sintered pellets of LCO and LLZTO were prepared independently. An Au electrode was fabricated on one side of each pellet using a DC sputter coater (SC-701 MKⅡ Advance, Sanyu electron) in a glove box. The LLZTO and LCO pellets with Au electrodes are stacked in an electrochemical cell, as shown in Fig. S3. The OCV measurement was taken using a multichannel Potentio-/Galvano-stat (VMP-3, Biologic).

The interfacial resistance measurement was also performed by electrochemical impedance spectroscopy (EIS). We employed a cell configuration with Au | LLZTO | stainless-steel, SS (SUS-316L, Nilaco)-LxCO composite | SS. The SS powder improves the electrical conductivity of the LxCO pellet without a high-temperature sintering process. The SUS powder was pressed into a pellet of 10 mmφ at 255 MPa. A mixture of SS and LxCO (x=0.78, 0.9) powders on the SS pellet was placed and pressed at 255 MPa. The LLZTO sintered body was prepared by sintering at 1000 °C for 12 hours using as-calcined LLZTO powder at 900 °C. On one side of the LLZTO pellet, an Au electrode was fabricated after polishing the LLZTO surface with sandpaper. This fabricated LLZTO pellet was stacked on the SS-LxCO composite-SUS bilayer pellet and pressed at 127 MPa to form the Au | LLZTO | SS-LxCO composite | SS quartet-layered pellet. EIS measurements from 1 MHz to 10 mHz were acquired at room temperature. AC amplitude was set

to 10 mV and DC potential was kept equal to the OCV during the measurement. The annealing treatment of the quartet-layered pellet was applied in Ar atmosphere for 3 hours.

## RESULTS AND DISCUSSION

Figure 1 shows high-temperature in-situ XRD patterns of the LLZTO and the LCO composite up to 900 °C taken every 100 °C. These diffraction patterns show that LLZTO and LCO are continuously observed from room temperature to 900 °C. In the case of the stoichiometric LCO, any decomposed products of LLZTO or LCO were not detected even up to 900 °C, which is consistent with previous literature [5,8].

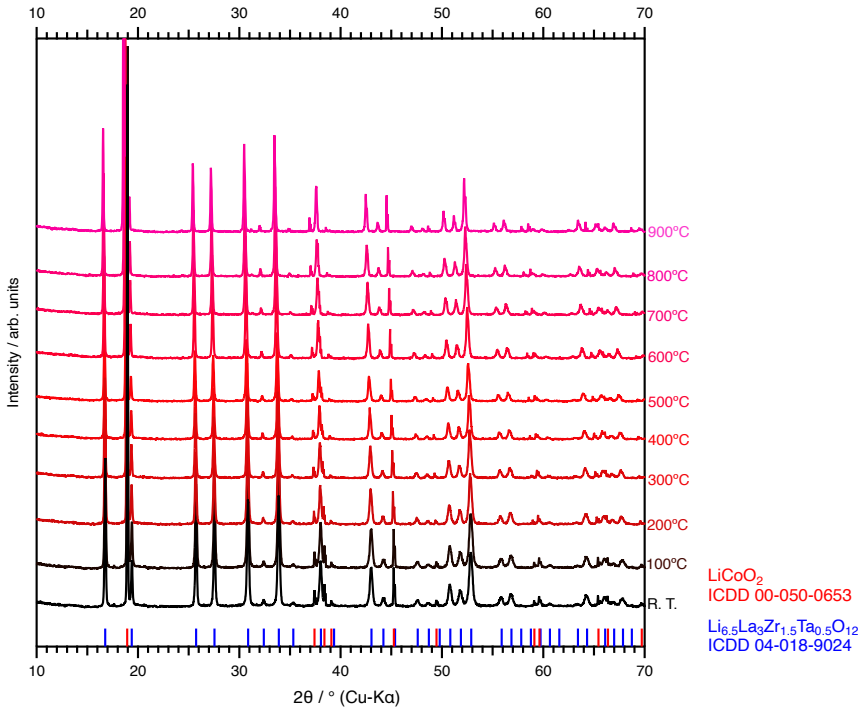


Figure 1. In-situ XRD patterns of composite pellets of the lithium-ion conductor $Li_{6.4}La_3Zr_{1.4}Ta_{0.6}O_{12}$ (LLZTO) and the cathode active material $LiCoO_2$ (LCO) heating from room temperature to 900 °C.

Figure 2 shows in-situ XRD patterns of LLZTO and $Li_xCoO_2$ (x≒0.55, LxCO). The LxCO immediately reacts with the LLZTO, as shown in Fig. 2a. The onset temperature of the reaction is 80 °C. The peak assigned to LxCO 003 reflection shifts toward higher angles between 80–180 °C (Fig. 2b), resulting in the stoichiometric LCO formation. A small shoulder appeared on the peak profile of LxCO 003 reflection on the high-angle side at 80 °C. This suggests lattice shrinkage along the c-axis with lithium insertion into the layered structure. With increasing temperature, the peak gradually shifts to a higher angle associated with broadening the profiles. The broadened peak splits at 110 °C, and the peak intensity at the higher angle gradually increases. Eventually, the peaks merge into one at 180 °C. The broadened peak is attributed to the inhomogeneous interface reactions due to nonuniform interparticle contacts between LxCO and LLZTO. Besides the peak shift of the LxCO, the peak intensity ascribed to LLZTO slightly increased during the heating process up to 200 °C and then decreased at the temperature above 200 °C (see Fig. 2a). We suspect the intensity change could be attributed to the atomic rearrangement of the lithium and oxygen in the LLZTO by the lithium and oxygen vacancy formations. The peaks corresponding to LLZTO gradually decayed during the subsequent heating process and mostly disappeared at 500 °C. The decomposed products of LLZTO exhibit poor crystallinity without long-range atomic rearrangement. Hence the characterization of the decomposed LLZTO becomes difficult by XRD measurements. Since the crystallization of the $La_2Zr_2O_7$, the preferred product of the phase-separated LLZTO is not observed at 500 °C, diffusions of the transition metal ions are still negligible. The decomposition of LLZTO ≤500 °C indicates that the lithium insertion into LxCO to form the LCO discussed above corresponds to the lithium extraction from the LLZTO. Consequently, a lithium-deficient LLZTO is formed.

Figure S4 shows the integrated peak intensities of LCO 003 and 104 reflections in LLZTO and LxCO mixture up to 900 °C. The LCO does not offer any changes from 200 °C to 400 °C. Then the peak intensities corresponding to the 003 reflection rapidly increase from 400 °C to 500 °C. We assume that the improvement in crystallinity is due to the decrease in stacking faults of LCO because only the 003 peak showed significant increase compared with the 104 peak. Subsequently, the peak intensities correspond to the LCO drastically decreasing at 600 °C, indicating the decomposition of LCO occurs above 500 °C. The crystallization of other oxide phases, such as Li-poor phases like $La_2Zr_2O_7$ and $LaCoO_3$, are observed due to the inter-diffusion of transition metals only above 600 °C. The detection of $La_2Co_2O_5$ indicates Co reduction accompanying $O_2$ gas evolution at a higher temperature. The CoO and $Co_3O_4$ derived from LCO are also detected because of compositional deficiencies such as Li evolution and transition metal migration. The possible reaction steps above are summarized as follows. In the low-temperature range below 200 °C, Li migration from LLZTO into LxCO is observed. Along with the lithium migration, the lithium-deficient LLZTO is formed from 80 °C to 180 °C. The lithium-deficient LLZTO decomposes above 200 °C without the interdiffusion of transition metals between the LLZTO and LCO. The interdiffusions of the transition metals are observed above 500 °C. The reaction products crystallize above 600 °C.

This decomposition of LLZTO occurs at much lower temperatures than the temperature range for highly resistive layer formation via transition metal interdiffusion reported in previous studies. This result suggests that the structural evolution of LLZTO is the origin of the highly resistive layer formation.

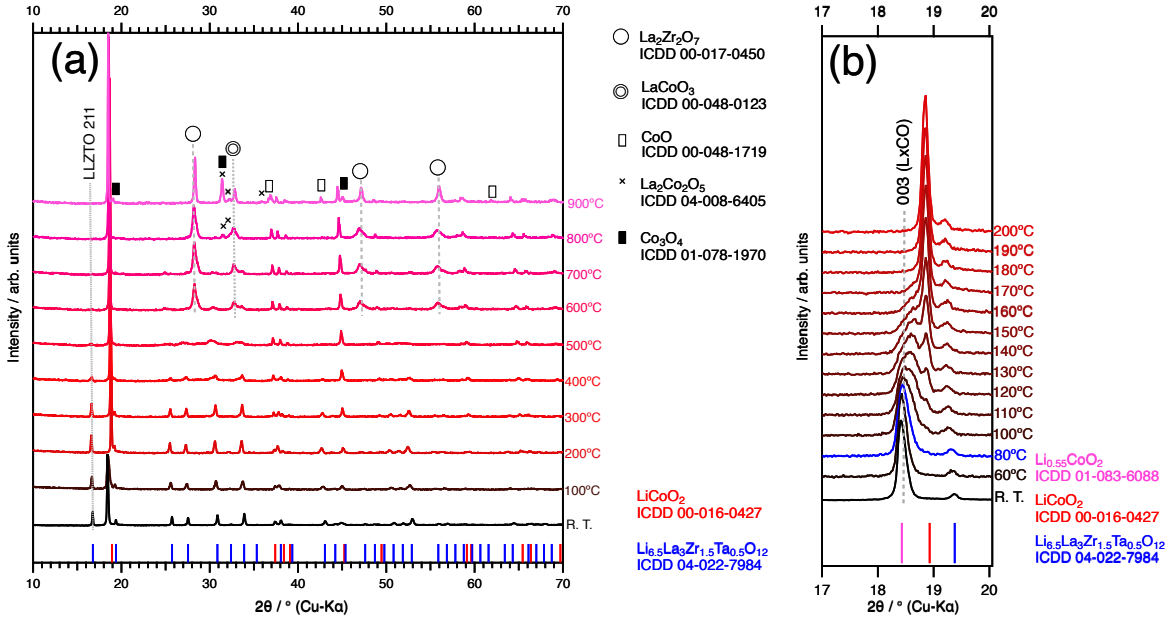


Figure 2. In-situ XRD patterns of the composite pellets of LLZTO and delithiated $LiCoO_2$ (LxCO, $x \fallingdotseq 0.55$) powder mixture calcined from room temperature up to 900 °C (a). Detailed LxCO 003 profiles change up to 200 °C (b).

Figure 3 shows the relative peak intensity of the LLZTO 211 reflection during the heating process normalized with room temperature. The peak intensity change is negligible in the case only LLZTO is calcined. A similar trend is observed in LLZTO and LCO mixture. The negligible intensity changes show that the bulk LLZTO is thermally stable against LCO up to 900 °C. On the other hand, the LLZTO and LxCO mixture exhibited completely different behavior. The integrated peak intensity of LLZTO 211 reflection increases from R.T. to 200 °C and subsequently decreases

at higher temperature regions. Eventually, the peak disappears above 500 °C. The initial increase of the peak intensity is probably due to the oxygen vacancy formation upon lithium extraction from LLZTO because the Li migration from LLZTO into LxCO has been finished up to 180 °C. (See Fig 2 (b)) Considering the possible oxygen loss along with the lithium migration, we also simulated powder XRD patterns for the oxygen- and lithium-deficient LLZTO using VESTA software [26], and compared the simulated results with the experimental data. Since we found that the intensity of the LLZTO 211 reflection peak: $I_{211}$ and 420 peak: $I_{420}$ slightly changed via the introduction of the oxygen- and lithium- vacancies, the $I_{211}/I_{420}$ values calculated via simulation and experimental data are summarized in Table S1. The simulation results showed that the $I_{211}/I_{420}$ value increased with the introduction of both oxygen- and lithium- vacancies. Among the experimental results, the $I_{211}/I_{420}$ value increases only in case the LLZTO and LxCO mixture at 100–200 ºC. Therefore, we assume that the oxygen loss from LLZTO simultaneously occurs during the lithium migration from LLZTO to LxCO. We also think oxygen loss is necessary to compensate for the charges in the LLZTO. After the lithium migration with oxygen loss, the oxygen- and lithium-deficient garnet structure gradually collapses with increasing temperature.

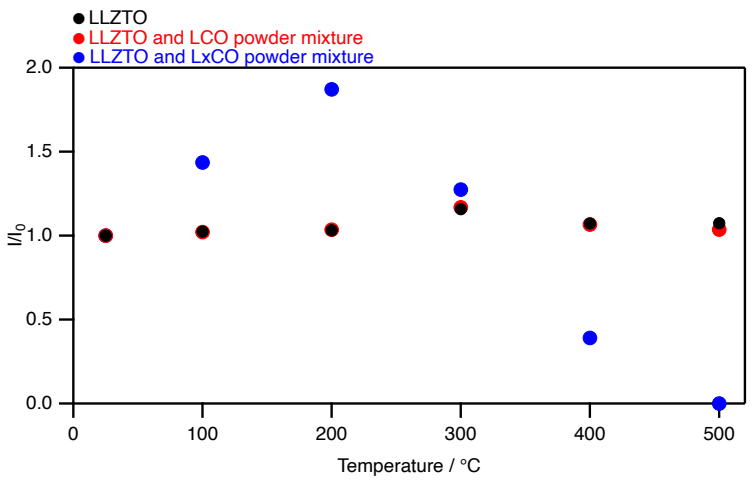


Figure 3. The relative peak intensity of the LLZTO 211 reflection at each temperature during the heating process normalized with the intensity at room temperature. The black, red, and blue dots show each value of LLZTO, LLZTO–LCO mixture, and LLZTO–LxCO mixture, respectively.

Ex-situ XRD measurements are conducted to confirm the influence of heating duration compared to in-situ XRD measurements. The ex-situ XRD diffraction patterns of the LCO and LLZTO mixture calcined every 100 °C are shown in Fig. S5. Even with the long calcination time of 12 hours, the LLZTO and LCO are maintained up to 900 °C. This result indicates that the interdiffusions of the transition metals between the LLZTO and LCO are negligible.

The ex-situ XRD patterns of the LLZTO and LxCO mixture are shown in Fig. S6. Similar trends are also observed regardless of heating duration. The results show that the reactions between LLZTO and LxCO are completed within 3 hours because of the fast Li diffusion. The ex-situ XRD results are consistent with the in-situ results until 150 °C and slightly different above 500 °C. The initial LCO formation by Li migration into LxCO is observed below 100 °C. (Fig. S6(b) The peak intensity of the LLZTO 211 reflection increased to 150 °C and decreased above 200 °C. (Fig.

S6(a)) Another complex oxide, $Co_2La_3TaO_9$, is observed above 700 °C. Long heating duration provides sufficient time for the atomic rearrangement of transition metals, especially in Ta diffusion, resulting in a thermodynamically stable phase.

We also investigated the elemental distribution across the LxCO-LLZTO interface to confirm the interdiffusion of transition metals. Figure 4 shows SEM-EDX line scans of LLZTO and LCO composite calcined particles at various calcination temperatures. The La, Zr, and Ta distributions show similar profiles at 200 °C, suggesting that the garnet phase is maintained after the lithium extraction. The garnet phase loses its crystallinity from 200 °C to 500 °C, and the distributions of the transition metals in LLZTO slightly changed, especially near the LCO-LLZTO interface. The trace of an interdiffusion of these transition metals at 500 °C agrees with the XRD study discussed above. Once the temperature reaches 900 °C, the line profiles of La, Zr, and Ta exhibit different distributions, showing the phase-separation of LLZTO.

Furthermore, a strong signal of the Co profile at the LLZTO side also shows a significant Co diffusion into the garnet phase. Combined with the XRD analysis (see Fig. 2), line analysis shows that lithium extraction's primary reaction <500 °C is the LLZTO decomposition. The transition metal interdiffusion subsequently occurs above 500 °C and the crystallization of reactants above 600 °C.

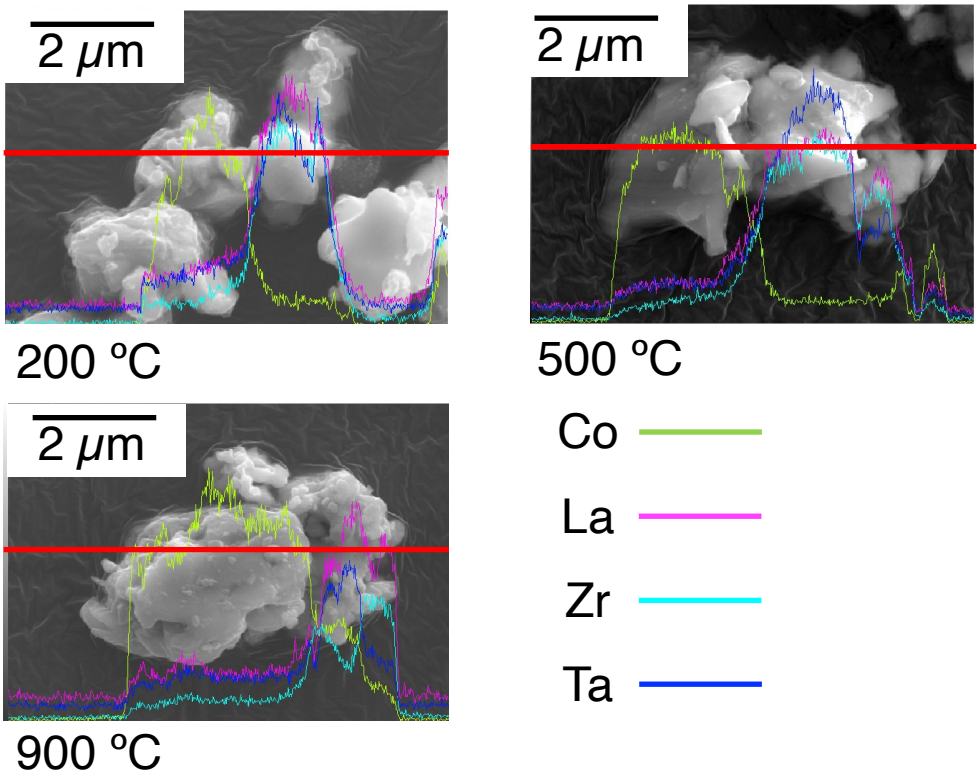


Figure 4. SEM-EDX line scans of the LLZTO and LCO interphase calcined at 200 °C, 500 °C, and 900 °C. The blown, blue, light blue, and pink lines correspond to Co, Ta, La, and Zr, respectively.

Thermodynamics of the LLZTO–LxCO interfacial reaction

We calculated the reaction Gibbs energy of LLZTO and LxCO (x=0.5) to validate the lithium extraction from LLZTO and LCO formation using DFT calculation data from Materials Project [27–30]. Since the phase separation of LLZTO is complicated, we chose lithium oxide ($Li_2O$) to replace the LLZTO because the stable $\mu_{Li}$ range in the $Li_2O$ mostly overlaps with that in LLZTO. We think the $Li_2O$ also worked as a lithium source for the LCO formation and calculated the Gibbs energy of the following reaction.

$$2Li_{0.5}CoO_2 + Li_2O \rightarrow 2LiCoO_2 + \frac{1}{2}Li_2O_2 \rightarrow 2LiCoO_2 + \frac{1}{2}Li_2O + \frac{1}{4}O_2 \quad (2)$$

Since the calculated Gibbs energy of the reaction is a negative value of -1.03 eV, the reaction is supposed to proceed spontaneously. This reaction requires the oxidation of LLZTO associated with the reduction of LxCO; hence, the reaction progresses with oxygen evolution via the phase separation of LLZTO. The oxygen evolution agrees with the above discussion concerning Fig. 3 and Table S1. Furthermore, the delithiated LxCO drastically reacts to LLZTO at a low temperature of 80°C, while LCO exhibits no predominant reaction with LLZTO. These reactivity differences are described by the lithium chemical potential gap ($\mu_{Li}$) at the LCO(or LxCO)-LLZTO interface. Thermodynamic properties of interfaces between two materials depend on the electrochemical potential of mobile ions and electrons[31]. The thermodynamic stabilities are attributed to the sum of each electrochemical potential in the case of mixed ion-electric conductors. The difference in the chemical potential gap of lithium at the interface could be the primary driving force for lithium migration and phase separation. If $\Delta\mu_{Li}$ at the interface is enough high, we suppose the lithium migration should occur at a lower temperature. Therefore, we also investigated the LxCO-LLZTO reaction at lower temperatures, as shown in Fig. S7. The long heating duration of 12 hours enabled the lithium migration at 60 °C. The result indicates that the onset temperature depends on the reaction kinetics.

We suspect the reported self-discharge and/or poor coulombic efficiency of LLZTO/LCO batteries at elevated temperatures are initiated by the spontaneous lithium migration discussed above[32,33]. Kim et al. fabricated a Li/LLZO/LCO cell using two types of LLZO and measured the

open circuit voltage after charging the cell to 4.05 V. Even with the improved electrochemical properties, the cell voltage continuously dropped for 2 hours[32]. Ye et al. fabricated LCO/LLZO composite cathode via a tape casting process and cycled the cell at 60 °C. The cell showed a coulombic efficiency of 60% at the 1st cycle and 90-95% during the following cycles.

A theoretical study also supports the instability of the LLZTO against LxCO. Nolan A. et al. reported[13] the calculated stability ranges for various solid electrolytes and cathode active materials to be represented by a potential window (0 eV / atom vs. lithium metal). Since LCO has a $\mu_{Li}$ stability range, which overlaps with $Li_7La_3Zr_2O_{12}$ (LLZO), the $\mu_{Li}$ in both LCO and LLZO stays within the potential window. On the other hand, the $\mu_{Li}$ in $Li_{0.5}CoO_2$ does not overlap with that of LLZO. Thus, the $Li_{0.5}CoO_2$ preferably absorbs lithium from LLZO to achieve equilibrium of $\mu_{Li}$.

Through electrochemical measurement, we attempted to prove the predicted relationship of $\mu_{Li}$ between LLZTO and LxCO. Gerischer et al. described the chemical potential corresponding to the total Gibbs free energy ($\Delta G_{total}$) of the reaction as follows[31].

$$\Delta G_{total} = -e\Delta V \quad (3)$$

Here, the $\Delta V$ is the open circuit voltage (OCV), and *e* represents the elementary charge. Hence, we measured the OCV to estimate the magnitude relationship of lithium chemical potential ($\mu_{Li}$) between LLZTO and LCO. The LLZTO exhibits 0.6 V lower than LCO, as shown in Fig. S3. The measured OCV value of 0.6-0.7 V is consistent with the theoretical calculation results [34,35]. Since the electrode potential of LCO is higher than LLZTO, the LLZTO has higher $\mu_{Li}$ than LCO. The $\Delta\mu_{Li}$ between LLZTO and LxCO becomes even more significant than that between LLZTO and LCO. The enormous interfacial $\mu_{Li}$ gap accelerates the Li migration and the phase transition. To

summarize the above, the interfacial $\mu_{Li}$ gap triggers the Li migration from LLZTO into LxCO, and the metastable Li-deficient LLZTO formation results in the phase separation at the relatively low temperature of <500 °C. Hence, we think the decomposed products of the LLZTO are the origin of the highly resistive layer rather than the layer formed by the interdiffusion of transition metals.

In parallel with the proposed reactions above, the phase separation of delithiated LxCO could be a competitive side reaction during heat treatment. The LxCO is easily decomposed to LCO and $Co_3O_4$, accompanied by oxygen release on thermal treatments, as shown in equation (4) [36].

$$Li_xCoO_2 \rightarrow xLiCoO_2 + \frac{1-x}{3}Co_3O_4 + \frac{1-x}{3}O_2 \qquad (4)$$

In addition, the obtained spinel $Co_3O_4$ also reacts with lithium to form a Spinel-type $Li_2Co_2O_4$ at a low temperature of <450 °C in case lithium sources are available. Subsequently, the Spinel-type $Li_2Co_2O_4$ transforms to the layered LCO during heating. In the present system, the LLZTO could become the lithium source, and the $Co_3O_4$ formed via the phase separation could react with the LLZTO to form a layered LCO. Hence, we also investigated the reactivity between the phase-separated LxCO and LLZTO.

Figure 5 exhibits the phase separation process of LxCO during the calcination up to 400 °C. Since the measurement is performed under an argon atmosphere, the final product after the phase separation is a layered LCO and a rocksalt CoO. The CoO formation around 200 °C suggests that the oxygen evolution occurs associated with the phase separation, as shown in Fig. 5(a). The onset temperature of the phase separation is at 150 °C, as shown in Fig. 5 (b). The slight peak shift of

the LxCO 003 reflection is first observed at 150 °C, and the continuous peak shift mostly finishes at 180 °C. The onset temperature of the LxCO phase separation at 150 °C is enough higher than the temperature of lithium migration from LLZTO to LxCO discussed in Fig. 2.

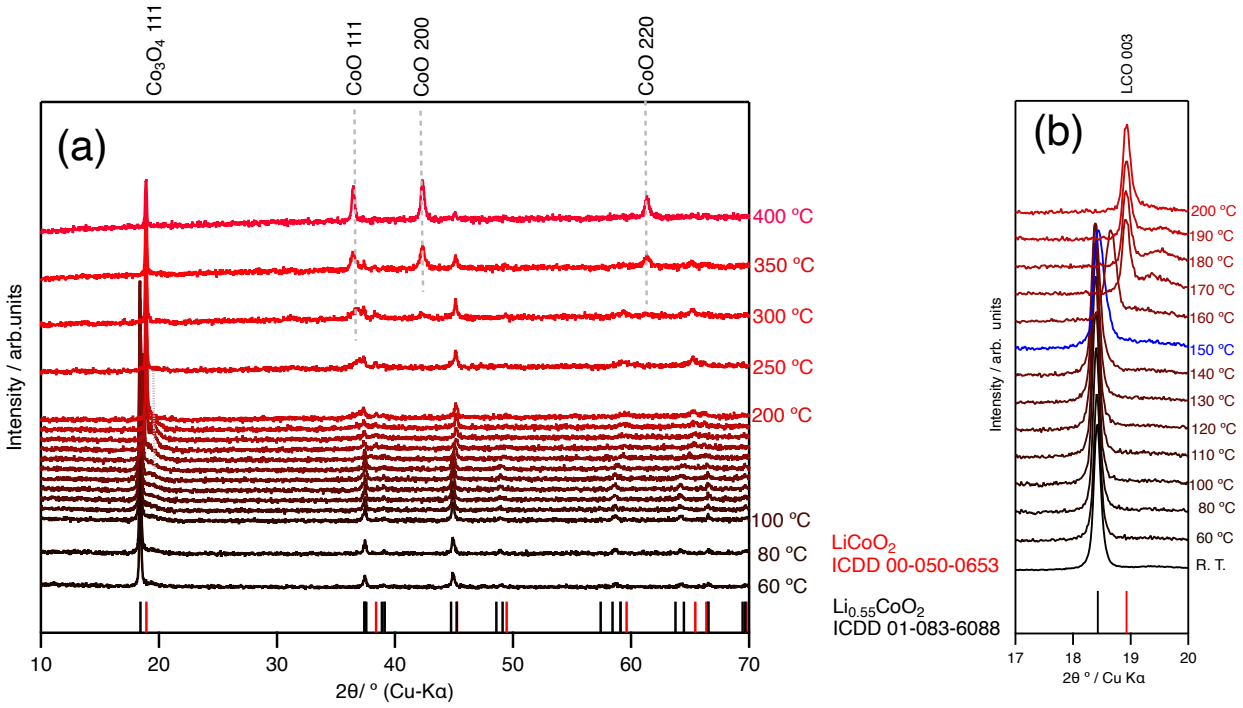


Figure 5. In-situ XRD results for the phase separation behavior of LxCO during the heating process up to 400 °C (a). The phase separation at the low temperature ranges up to 200 °C (b).

Figure 6 (a) shows in situ XRD patterns of the reaction for the LLZTO and the phase-separated LxCO mixture. No significant reaction is observed even up to 600 °C. Figure 6 (b) shows the relative peak intensities at each calcination temperature to a room temperature value. Since the integrated peak intensity of the 211 reflection peak of LLZTO and the 311 reflection peak of $Co_3O_4$

showed negligible intensity changes up to 600 °C, the phase separation of LxCO is negligible for the interfacial reaction between LLZTO and LxCO.

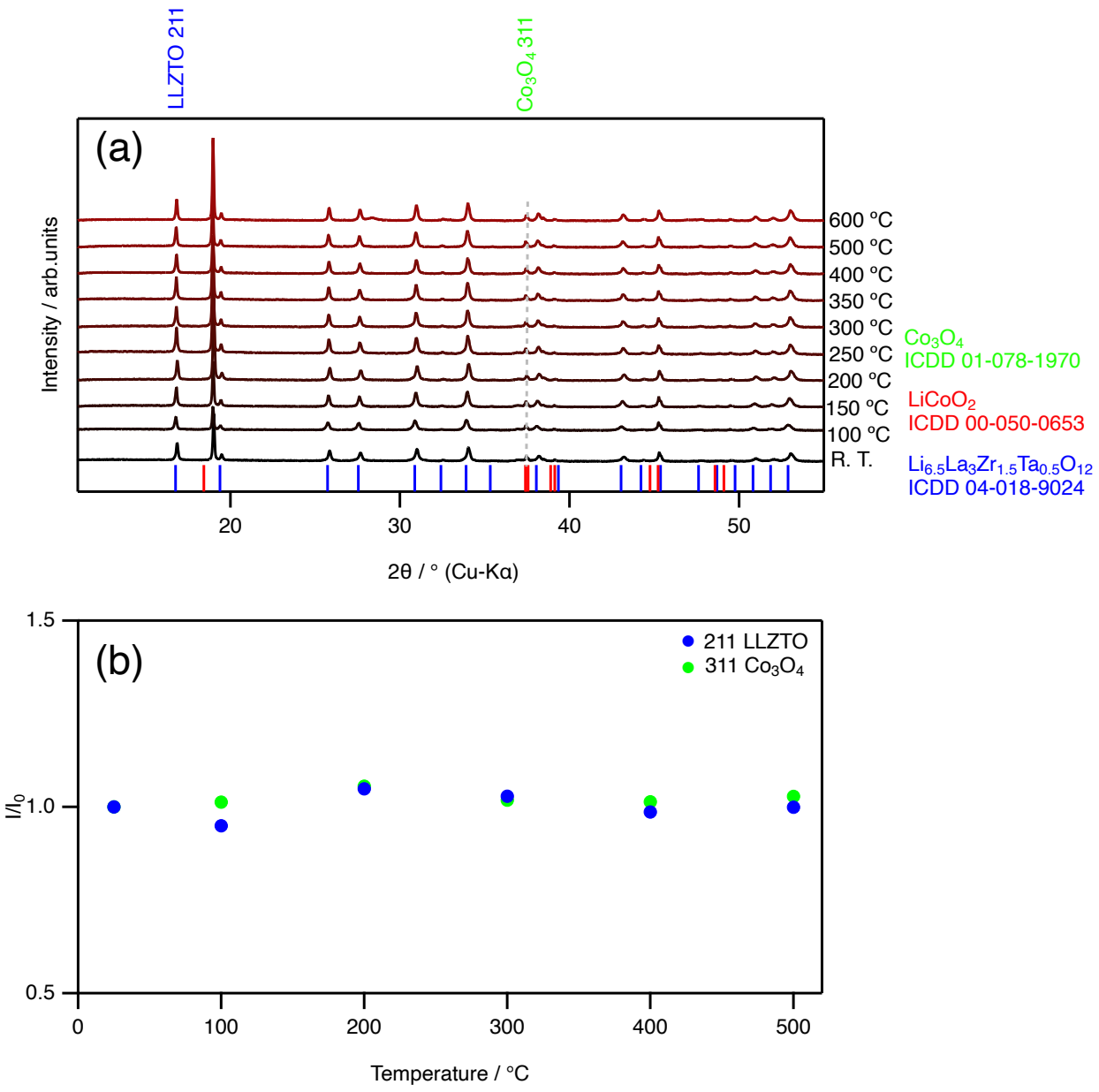


Figure 6. Ex-situ XRD patterns of LLZTO and a phase-separated LxCO powder calcined from room temperature to 600 °C (a). The relative peak intensity changes of LLZTO and phase-separated LxCO mixture (b). The peak intensities are normalized with the intensity at room

temperature. The blue and light green dots correspond to the 211 reflection in LLZTO and the 311 reflection in $Co_3O_4$, respectively.

EIS measurement for the highly resistive layer formation process

Electrochemical impedance spectroscopy (EIS) was used to assess the resistance across the LxCO | LLZTO interface on charge transport due to the chemical and structural changes presented above. Fig. 7 shows Nyquist plots for an Au | LLZTO | LxCO-SS | SS cell with different annealing conditions. The as-prepared cell, before annealing, had a single semicircle whose vertex had a frequency of 3 kHz. We think the semicircle corresponds to the charge transfer resistance at the LLZTO | LxCO interface regarding the reported frequency ranges of the LLZTO | LCO interfacial resistance [37,38]. In addition, the Au | LLZTO | Au symmetric cell showed a small semicircle at a higher frequency region (see Fig. S8). The high interfacial resistance of 100 kΩ is caused by poor LLZTO | LxCO interface contact without heat treatment. The interfacial resistance approximately doubled after the heat treatment at 100 °C. The increased interfacial resistance indicates that the lithium- and oxygen-deficient LLZTO forms the highly resistive layer. In the case of 200 °C annealing, the sample exhibited an additional component at lower frequencies, around 30 Hz, suggesting a secondary-phase formation. These increases in resistance support the XRD structural changes below 200 °C. Spontaneous lithium migration triggered by $\mu_{Li}$ gap at the LxCO-LLZO could result in detrimental electrochemical properties.

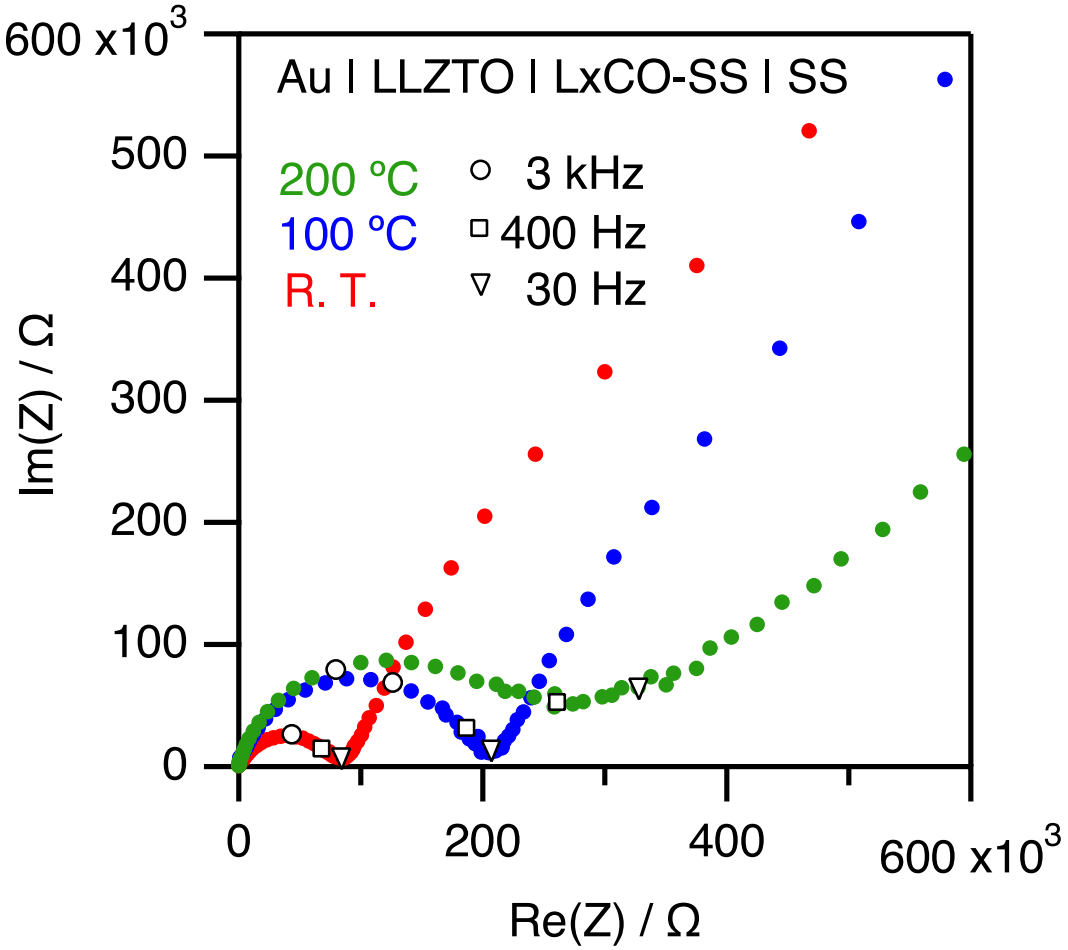


Figure 7. Nyquist plot of an Au | LLZTO | LxCO-SS | SS cell before and after annealing.

Based on the discussion above, we conclude that the major component of the highly resistive layer at the LLZTO-LCO interface is the decomposed LLZTO rather than the interdiffusion layer of the transition metals. The trigger of the reaction is the lithium migration from LLZTO to LxCO at a low temperature of 60 °C with a negligible LxCO phase separation, which is the competing side reaction. The driving force of the lithium migration is the chemical potential gap $\Delta\mu_{Li}$ between LLZTO and LxCO. During the Li migration, the oxygen vacancies are introduced in the lithium-

and oxygen-deficient LLZTO to compensate for the charges up to 200 °C. The structural collapse of the lithium- and oxygen-deficient LLZTO occurs above 200 to 500 °C due to the increased lithium- and oxygen vacancies with increased driving force at the elevated temperature. The interdiffusion of transition metals is observed above 600 °C. Therefore, the materials design to minimize the $\Delta\mu_{Li}$ at the solid-solid interface become the crucial technology for developing all-solid-sate lithium batteries.

## CONCLUSIONS

In this study, we investigated the highly resistive layer formation at the LCO | LLZTO interface during the heating process using in-situ and ex-situ X-ray diffraction. We compared a stoichiometric LCO and a chemically delithiated LxCO with different Li chemical potential gaps at the cathode | electrolyte interface to determine the trigger of the interfacial degradation behavior. In the case of LCO with stoichiometric composition, no detectable reactive phase formation with LLZTO was observed even at 900 °C, consistent with previous literature[5,8.] In comparison, the chemically delithiated LxCO ($x \fallingdotseq 0.55$) shows Li migration even at 80 °C, much lower than the decomposition temperature of LxCO. The peak assigned to the 003 reflections of LxCO gradually shifted to a higher angle at 80-200 °C, showing the stoichiometric LCO formation. Besides the stoichiometric LCO formation, we confirmed increasing of interfacial resistance at 100 to 200 °C by EIS measurements. The integrated peak intensity corresponding to LLZTO decreased. The LCO formation suggests that LCO is formed by the migration of Li from LLZTO to LxCO, triggered by the difference in the chemical potentials of Li in LLZTO and LCO, and at the same time, lithium- and oxygen-deficient LLZTO leads to phase separation.

Furthermore, the peak ascribed to LLZTO almost disappeared at 500 °C. Then the other crystalline oxide phases, such as $La_2Zr_2O_7$ and $LaCoO_3$, appeared at higher temperatures >500 °C, suggesting that the interdiffusion of the transition metal ions occurs only above 500 °C. The result agrees with the EDX analysis. The present study exhibits that the origin of the highly resistive layer at the LLZTO-LCO interface is not the interdiffusion of transition metals but the decomposition of the garnet phase triggered by lithium extraction. These results offer that the chemical potentials of the carrier ions are the most critical parameter for the materials design of the solid-solid interface.

REFERENCES


(1) Gao, Z.; Sun, H.; Fu, L.; Ye, F.; Zhang, Y.; Luo, W.; Huang, Y. Promises, Challenges, and Recent Progress of Inorganic Solid-State Electrolytes for All-Solid-State Lithium Batteries. *Advanced Materials*. **2017**, 30, 1705702.

(2) Murugan, R.; Thangadurai, V.; Weppner, W. Fast Lithium Ion Conduction in Garnet-Type $Li_7La_3Zr_2O_{12}$. *Angewandte Chemie* **2007**, *46*, 7778–7781.

(3) Wang, C.; Fu, K.; Kammampata, S. P.; McOwen, D. W.; Samson, A. J.; Zhang, L.; Hitz, G. T.; Nolan, A. M.; Wachsman, E. D.; Mo, Y.; Thangadurai, V.; Hu, L. Garnet-Type Solid-State Electrolytes: Materials, Interfaces, and Batteries. American Chemical Society **2020**, 120, 4257–4300.

(4) Ren, Y.; Wachsman, E. D. All Solid-State Li/LLZO/LCO Battery Enabled by Alumina Interfacial Coating. *J Electrochem Soc* **2022**, *169*, 040529.

(5) Uhlenbruck, S.; Dornseiffer, J.; Lobe, S.; Dellen, C.; Tsai, C. L.; Gotzen, B.; Sebold, D.; Finsterbusch, M.; Guillon, O. Cathode-Electrolyte Material Interactions during Manufacturing of Inorganic Solid-State Lithium Batteries. *J Electroceram* **2017**, *38*, 197–206.

(6) Tsai, C. L.; Ma, Q.; Dellen, C.; Lobe, S.; Vondahlen, F.; Windmüller, A.; Grüner, D.; Zheng, H.; Uhlenbruck, S.; Finsterbusch, M.; Tietz, F.; Fattakhova-Rohlfing, D.; Buchkremer, H. P.; Guillon, O. A Garnet Structure-Based All-Solid-State Li Battery without Interface Modification: Resolving Incompatibility Issues on Positive Electrodes. *Sustain Energy Fuels* **2019**, *3*, 280–291.

(7) Kato, T.; Hamanaka, T.; Yamamoto, K.; Hirayama, T.; Sagane, F.; Motoyama, M.; Iriyama, Y. In-Situ $Li_7La_3Zr_2O_{12}/LiCoO_2$ Interface Modification for Advanced All-Solid-State Battery. *J Power Sources* **2014**, *260*, 292–298.

(8) Ren, Y.; Liu, T.; Shen, Y.; Lin, Y.; Nan, C. W. Chemical Compatibility between Garnet-like Solid State Electrolyte $Li_{6.75}La_3Zr_{1.75}Ta_{0.25}O_{12}$ and Major Commercial Lithium Battery Cathode Materials. *Journal of Materiomics* **2016**, *2*, 256–264.

(9) Kim, Y.; Kim, D.; Bliem, R.; Vardar, G.; Waluyo, I.; Hunt, A.; Wright, J. T.; Katsoudas, J. P.; Yildiz, B. Thermally Driven Interfacial Degradation between Li7La3Zr2O12 Electrolyte and $LiNi_{0.6}Mn_{0.2}Co_{0.2}O_2$ Cathode. *Chemistry of Materials* **2020**, *32*, 9531–9541.

(10) Vardar, G.; Bowman, W. J.; Lu, Q.; Wang, J.; Chater, R. J.; Aguadero, A.; Seibert, R.; Terry, J.; Hunt, A.; Waluyo, I.; Fong, D. D.; Jarry, A.; Crumlin, E. J.; Hellstrom, S. L.; Chiang, Y. M.; Yildiz, B. Structure, Chemistry, and Charge Transfer Resistance of the Interface between $Li_7La_3Zr_2O_{12}$ Electrolyte and $LiCoO_2$ Cathode. *Chemistry of Materials* **2018**, *30*, 6259–6276.

(11) Kim, K. H.; Iriyama, Y.; Yamamoto, K.; Kumazaki, S.; Asaka, T.; Tanabe, K.; Fisher, C. A. J.; Hirayama, T.; Murugan, R.; Ogumi, Z. Characterization of the Interface between

$LiCoO_2$ and $Li_7La_3Zr_2O_{12}$ in an All-Solid-State Rechargeable Lithium Battery. *J Power Sources* **2011**, *196*, 764–767.

(12) Park, K.; Yu, B. C.; Jung, J. W.; Li, Y.; Zhou, W.; Gao, H.; Son, S.; Goodenough, J. B. Electrochemical Nature of the Cathode Interface for a Solid-State Lithium-Ion Battery: Interface between $LiCoO_2$ and Garnet-$Li_7La_3Zr_2O_{12}$. *Chemistry of Materials* **2016**, *28*, 8051–8059.

(13) Nolan, A. M.; Wachsman, E. D.; Mo, Y. Computation-Guided Discovery of Coating Materials to Stabilize the Interface between Lithium Garnet Solid Electrolyte and High-Energy Cathodes for All-Solid-State Lithium Batteries. *Energy Storage Mater* **2021**, *41*, 571–580.

(14) Ohta, S.; Komagata, S.; Seki, J.; Saeki, T.; Morishita, S.; Asaoka, T. Short Communication All-Solid-State Lithium Ion Battery Using Garnet-Type Oxide and $Li_3BO_3$ Solid Electrolytes Fabricated by Screen-Printing. *J Power Sources* **2013**, *238*, 53–56.

(15) Ohta, S.; Seki, J.; Yagi, Y.; Kihira, Y.; Tani, T.; Asaoka, T. Co-Sinterable Lithium Garnet-Type Oxide Electrolyte with Cathode for All-Solid-State Lithium Ion Battery. *J Power Sources* **2014**, *265*, 40–44.

(16) Liu, T.; Ren, Y.; Shen, Y.; Zhao, S. X.; Lin, Y.; Nan, C. W. Achieving High Capacity in Bulk-Type Solid-State Lithium Ion Battery Based on $Li_{6.75}La_3Zr_{1.75}Ta_{0.25}O_{12}$ Electrolyte: Interfacial Resistance. *J Power Sources* **2016**, *324*, 349–357.

(17) Wang, D.; Sun, Q.; Luo, J.; Liang, J.; Sun, Y.; Li, R.; Adair, K.; Zhang, L.; Yang, R.; Lu, S.; Huang, H.; Sun, X. Mitigating the Interfacial Degradation in Cathodes for High-Performance Oxide-Based Solid-State Lithium Batteries. *ACS Appl Mater Interfaces* **2019**, *11* (5), 4954–4961.

(18) Han, F.; Yue, J.; Chen, C.; Zhao, N.; Fan, X.; Ma, Z.; Gao, T.; Wang, F.; Guo, X.; Wang, C. Interphase Engineering Enabled All-Ceramic Lithium Battery. *Joule* **2018**, *2*, 497–508.

(19) Cheng, E. J.; Kushida, Y.; Abe, T.; Kanamura, K. Degradation Mechanism of All-Solid-State Li-Metal Batteries Studied by Electrochemical Impedance Spectroscopy. *ACS Appl Mater Interfaces* **2022**, *14*, 40881–40889.

(20) Richards, W. D.; Miara, L. J.; Wang, Y.; Kim, J. C.; Ceder, G. Interface Stability in Solid-State Batteries. *Chemistry of Materials* **2016**, *28*, 266–273.

(21) Kato, T.; Hamanaka, T.; Yamamoto, K.; Hirayama, T.; Sagane, F.; Motoyama, M.; Iriyama, Y. In-Situ $Li_7La_3Zr_2O_{12}$/$LiCoO_2$ Interface Modification for Advanced All-Solid-State Battery. *J Power Sources* **2014**, *260*, 292–298.

(22) Sastre, J.; Chen, X.; Aribia, A.; Tiwari, A. N.; Romanyuk, Y. E. Fast Charge Transfer across the $Li_7La_3Zr_2O_{12}$Solid Electrolyte/$LiCoO_2$Cathode Interface Enabled by an Interphase-Engineered All-Thin-Film Architecture. *ACS Appl Mater Interfaces* **2020**, *12*, 36196–36207.

(23) Gao, B.; Jalem, R.; Tateyama, Y. First-Principles Study of Microscopic Electrochemistry at the LiCoO2Cathode/LiNbO3Coating/β-Li3PS4Solid Electrolyte Interfaces in an All-Solid-State Battery. *ACS Appl Mater Interfaces* **2021**, *13*, 11765–11773.

(24) Matsui, M.; Takahashi, K.; Sakamoto, K.; Hirano, A.; Takeda, Y.; Yamamoto, O.; Imanishi, N. Phase Stability of a Garnet-Type Lithium Ion Conductor $Li_7La_3Zr_2O_{12}$. *Dalton Transactions* **2014**, *43*, 1019–1024.

(25) Hwang, J.; Takeuchi, K.; Matsumoto, K.; Hagiwara, R. NASICON: vs. Na Metal: A New Counter Electrode to Evaluate Electrodes for Na Secondary Batteries. *J Mater Chem A Mater* **2019**, *7*, 27057–27065.

(26) Momma, K.; Izumi, F. VESTA3 for Three-Dimensional Visualization of Crystal, Volumetric and Morphology Data. *J Appl Crystallogr* **2011**, *44*, 1272–1276.

(27) Ong, S. P.; Wang, L.; Kang, B.; Ceder, G. Li-Fe-P-$O_2$ Phase Diagram from First Principles Calculations. *Chemistry of Materials* **2008**, *20*, 1798–1807.

(28) Wang, A.; Kingsbury, R.; Mcdermott, M.; Horton, M.; Jain, A.; Ong, S. P.; Dwaraknath, S.; Persson, K. A. A Framework for Quantifying Uncertainty in DFT Energy Corrections. *Scientifc Reports* **2021**, 11, 15496

(29) Jain, A.; Hautier, G.; Ong, S. P.; Moore, C. J.; Fischer, C. C.; Persson, K. A.; Ceder, G. Formation Enthalpies by Mixing GGA and GGA + U Calculations. *Phys Rev B Condens Matter Mater Phys* **2011**, *84*, 045115.

(30) Aykol, M.; Dwaraknath, S. S.; Sun, W.; Persson, K. A. *Thermodynamic Limit for Synthesis of Metastable Inorganic Materials*; **2018**, 4, 148.

(31) Schuld, S.; Hausbrand, R.; Fingerle, M.; Jaegermann, W.; Weitzel, K. M. Experimental Studies on Work Functions of Li+ Ions and Electrons in the Battery Electrode Material $LiCoO_2$: A Thermodynamic Cycle Combining Ionic and Electronic Structure. *Adv Energy Mater* **2018**, *8*, 1703411.

(32) Kim, K. J.; Rupp, J. L. M. All Ceramic Cathode Composite Design and Manufacturing towards Low Interfacial Resistance for Garnet-Based Solid-State Lithium Batteries. *Energy Environ. Sci.* **2020**, *13*, 4930–4945.

(33) Ye, R.; Ihrig, M.; Figgemeier, E.; Fattakhova-Rohlfing, D.; Finsterbusch, M. Aqueous Processing of $LiCoO_2$–$Li_{6.6}La_3Zr_{1.6}Ta_{0.4}O_{12}$ Composite Cathode for High-Capacity Solid-State Lithium Batteries. *ACS Sustainable Chemistry & Engineering* **2023**, *11*, 5184–5194.

(34) Okuno, Y.; Haruyama, J.; Tateyama, Y. Comparative Study on Sulfide and Oxide Electrolyte Interfaces with Cathodes in All-Solid-State Battery via First-Principles Calculations. *ACS Appl Energy Mater* **2020**, *3*, 11061–11072.

(35) Abe, T.; Koyama, T. Thermodynamic Modeling of the $LiCoO_2$-$CoO_2$ Pseudo-Binary System. *CALPHAD* **2011**, *35*, 209–218.

(36) Baba, Y.; Okada, S.; Yamaki, J. Thermal Stability of $Li_xCoO_2$ Cathode for Lithium Ion Battery. *Solid State Ionics* **2002**, 148, 311-316.

(37) Sastre, J.; Chen, X.; Aribia, A.; N. Tiwari, A.; E. Romanyuk, Y. Fast Charge Transfer across the $Li_7La_3Zr_2O_{12}$ Solid Electrolyte/$LiCoO_2$ Cathode Interface Enabled by an Interphase-Engineered All-Thin-Film Architecture. *ACS Applied Materials & Interfaces* **2020**, *12* , 36196–36207.

(38) Vardar, G.; J. Bowman, W.; Lu, Q.; Wang, J.; J. Chater, R.; Aguadero, A.; Seibert, R.; Terry, J.; Hunt, A.; Waluyo, I.; D. Fong, D.; Jarry, A.; J. Crumlin, E.; L. Hellstrom, S.; Chiang, Y.-M.; Yildiz, B. Structure, Chemistry, and Charge Transfer Resistance of the Interface between $Li_7La_3Zr_2O_{12}$ Electrolyte and $LiCoO_2$ Cathode. *Chemistry of Materials* **2018**, *30*, 6259–6276.

## ASSOCIATED CONTENT

### Supporting Information

The Supporting Information is available free of charge at

Powder XRD patterns of the LLZTO and LxCO used in the present study.

Relative peak intensity changes of the LCO after the low-temperature reaction discussed in the present study.

Ex-situ XRD patterns of the LLZTO and LxCO interface for long-term reactions at elevated temperatures.

AUTHOR INFORMATION

Corresponding Author

Masaki Matsui – Department of Chemistry, Hokkaido University, Sapporo, Hokkaido 060-0810, Japan; orcid.org/0000-0003-1499-7457; E-mail: matsui@sci.hokudai.ac.jp

Authors

Kana Onoue – Graduate School of Chemical Science and Engineering, Hokkaido University, Sapporo, Hokkaido 060-0810, Japan

Akira Nasu – Department of Chemistry, Hokkaido University, Sapporo, Hokkaido 060-0810, Japan; orcid.org/ 0009-0002-7779-5721

Kazuhiko Matsumoto – Graduate School of Energy Science, Kyoto University, Kyoto 606-8501, JAPAN

Rika Hagiwara – Graduate School of Energy Science, Kyoto University, Kyoto 606-8501, JAPAN

Hiroaki Kobayashi– Department of Chemistry, Hokkaido University, Sapporo, Hokkaido 060-0810, Japan; orcid.org/0000-0001-6705-9515

ACKNOWLEDGMENTS

The authors thank Dr. Yoshitaka Tateyama at National Institute for Materials Science for his fruitful discussions. The present work was supported by KAKENHI of MEXT, Grant Number 19H05812 and 19H05813.

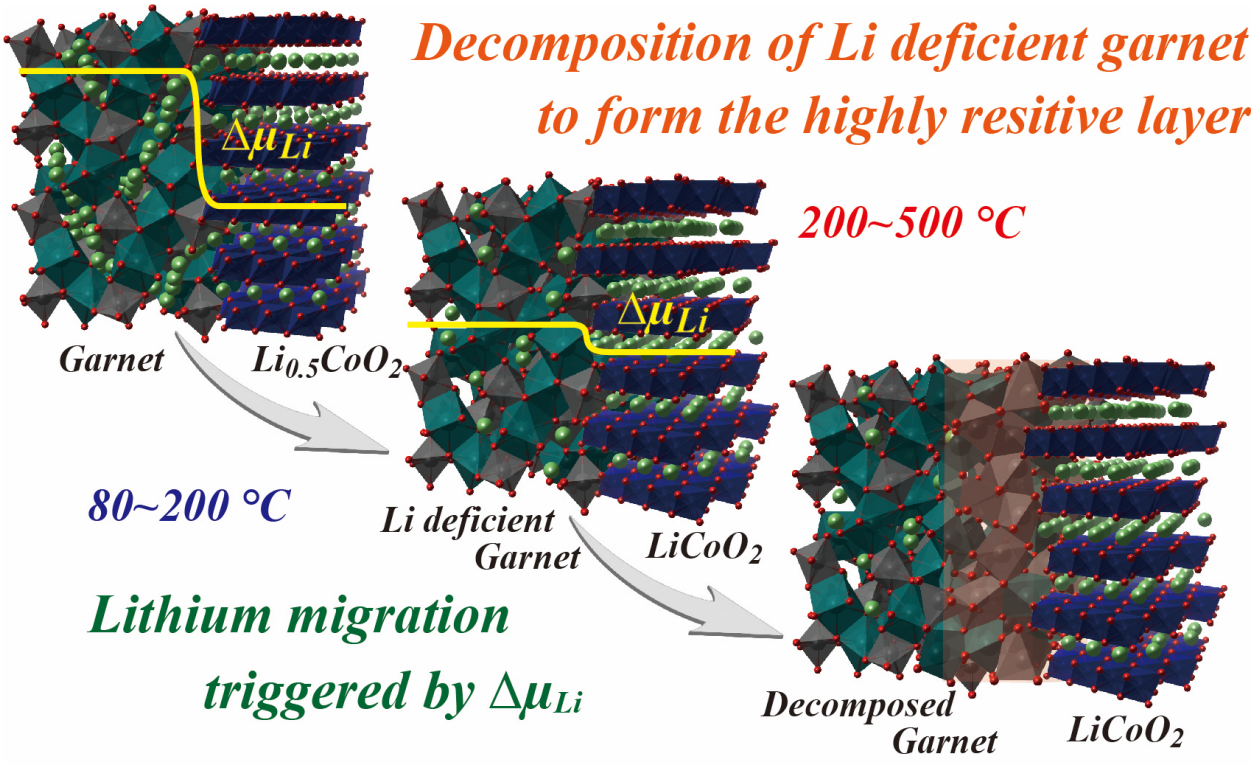
Decomposition of Li deficient garnet
to form the highly resitive layer
$\Delta\mu_{Li}$
Garnet
$Li_{0.5}CoO_2$
200~500 °C
$\Delta\mu_{Li}$
80~200 °C
Li deficient
Garnet
$LiCoO_2$
Lithium migration
triggered by $\Delta\mu_{Li}$
Decomposed
Garnet
$LiCoO_2$